JPhys Materials

PAPER • OPEN ACCESS

Anisotropic magnetic and transport properties of orthorhombic *o*-$Pr_2Co_3Ge_5$

To cite this article: Trent M Kyrk *et al* 2022 *J. Phys. Mater.* **5** 044007

Journal of Physics: Materials

PAPER

Anisotropic magnetic and transport properties of orthorhombic *o*-$Pr_2Co_3Ge_5$

Trent M Kyrk[1], Ellis R Kennedy[2], Jorge Galeano-Cabral[3,4], Kaya Wei[4], Gregory T McCandless[1], Mary C Scott[2,5,6], Ryan E Baumbach[4,7] and Julia Y Chan[1,*]

[1] Department of Chemistry and Biochemistry, Baylor University, Waco, TX 76706, United States of America
[2] Department of Materials Science and Engineering, University of California Berkeley, Berkeley, CA 94720, United States of America
[3] FAMU-FSU College of Engineering, Department of Mechanical Engineering, Florida State University, Tallahassee, FL 32310, United States of America
[4] National High Magnetic Field Laboratory, Florida State University, Tallahassee, FL 32310, United States of America
[5] Materials Sciences Division, Lawrence Berkeley National Laboratory, Berkeley, CA 94720, United States of America
[6] National Center for Electron Microscopy, Molecular Foundry, Lawrence Berkeley National Laboratory, Berkeley, CA 94720, United States of America
[7] Department of Physics, Florida State University, Tallahassee, FL 32310, United States of America
[*] Author to whom any correspondence should be addressed.

E-mail: Julia_Chan@baylor.edu

Keywords: crystal growth, lanthanides, magnetism, praseodymium

Supplementary material for this article is available online

OPEN ACCESS

RECEIVED
27 May 2022

REVISED
13 October 2022

ACCEPTED FOR PUBLICATION
17 October 2022

PUBLISHED
28 October 2022

Abstract

The crystal structure, electron energy-loss spectroscopy (EELS), heat capacity, and anisotropic magnetic and resistivity measurements are reported for Sn flux grown single crystals of orthorhombic $Pr_2Co_3Ge_5$ ($U_2Co_3Si_5$-type, *Ibam*). Our findings show that *o*-$Pr_2Co_3Ge_5$ hosts nearly trivalent Pr ions, as evidenced by EELS and fits to temperature dependent magnetic susceptibility measurements. Complex magnetic ordering with a partially spin-polarized state emerges near $T_{sp} = 32$ K, with a spin reconfiguration transition near $T_M = 15$ K. Heat capacity measurements show that the phase transitions appear as broad peaks in the vicinity of T_{sp} and T_M. The magnetic entropy further reveals that crystal electric field splitting lifts the Hund's rule degeneracy at low temperatures. Taken together, these measurements show that $Pr_2Co_3Ge_5$ is an environment for complex f state magnetism with potential strongly correlated electron states.

1. Introduction

The $Ln_2M_3X_5$ (Ln = lanthanide or actinide; M = transition metal; X = Ga, Si, Ge, Sn) family of intermetallic compounds is rich in complex magnetic and strongly correlated electron behavior. This includes charge density waves in $Sm_2Ru_3Ge_5$ and $Nd_2Ru_3Ge_5$ [1, 2], superconductivity in $Y_2Ir_3Ge_5$ and $La_2Ir_3Ge_5$ [3–5], Kondo lattice behavior in $Ce_2Rh_3Ge_5$, $Ce_2Ir_3Ge_5$, and $Yb_2Ir_3Ge_5$ [6–8], competition between ferromagnetic and antiferromagnetic ordering in $Pr_2Ni_3Si_5$, $Ho_2Ni_3Si_5$, and $Tb_2Co_3Ge_5$ [9–12], intermediate/mixed valance states in $Ce_2Co_3Ge_5$, $Ce_2Re_3Si_5$, and $Eu_2Pt_3Si_5$ [13–16], and pressure induced quantum critical behavior in $Ce_2Ni_3Ge_5$ [17, 18]. The $Pr_2M_3Ge_5$ (M = Co [19], Ni [20], Ru [19], Rh [19], Pd, Ir [3, 19], Pt) compounds show many exotic phenomena such as charge density waves and polymorphism in $Pr_2Ru_3Ge_5$ [1], heavy electron behavior in $Pr_2Rh_3Ge_5$ [21], and magnetoresistance of nearly ten-fold increase in $Pr_2Pd_3Ge_5$ [21], A superconducting transition has been observed in $Pr_2Pt_3Ge_5$ at $T_{SC} = 6.7$ K, coexisting with two antiferromagnetic transitions below $T = 5$ K [5, 22, 23] and non-Fermi liquid behavior, suggesting a field dependent quantum critical point [24].

The $Pr_2M_3Ge_5$ compounds crystallize in one of three structure types: the $Sc_2Fe_3Si_5$-type (*P*4/*mnc*) [25], $U_2Co_3Si_5$-type (*Ibam*) [26], and $Lu_2Co_3Si_5$-type (*C*2/*c* or *I*2/*c*) [27]. The orthorhombic $U_2Co_3Si_5$-type and monoclinic $Lu_2Co_3Si_5$-type structures are the most closely related and can be considered to be distorted coloring variants of the $BaAl_4$ structure type, manifesting as corrugated slabs of Ln-atoms layered between distorted [T_3X_5] tetrahedral slabs. The two structure types differ through a monoclinic distortion that results

in the angle β shifting from 90° in the $U_2Co_3Si_5$ structure type to 90° + δ in the $Lu_2Co_3Si_5$ structure type. As Ln becomes larger, the distortion angle δ becomes smaller, approaching 90° and, therefore, the $U_2Co_3Si_5$ structure type [19, 27]. For the $Ln_2Co_3Ge_5$ system, $La_2Co_3Ge_5$ and $Ce_2Co_3Ge_5$ crystallize in the $U_2Co_3Si_5$ structure type and Ln = Sm [19, 28], Gd—Er [12, 19, 29], and Y [19] crystallize in the $Lu_2Co_3Si_5$ structure type. $Pr_2Co_3Ge_5$ and $Nd_2Co_3Ge_5$ exist at the brink of the orthorhombic/monoclinic phase boundary and have been reported to crystallize in both structure types. The polymorphs of $Pr_2Co_3Ge_5$ in the $U_2Co_3Si_5$ [13, 30] and $Lu_2Co_3Si_5$ [19, 28] structure types are denoted here as *o*-$Pr_2Co_3Ge_5$ and *m*-$Pr_2Co_3Ge_5$, respectively. The difference between *o*-$Pr_2Co_3Ge_5$ and *m*-$Pr_2Co_3Ge_5$ is remarkably small, with β deviating from 90° in *o*-$Pr_2Co_3Ge_5$ to approximately 90.4° in *m*-$Pr_2Co_3Ge_5$. However small, the structural difference is reflected in the magnetic properties of these compounds.

Single crystals of *m*-$Pr_2Co_3Ge_5$ have been shown to exhibit complex magnetic behavior with two antiferromagnetic-like transitions at 33 K and 6 K along with strong sensitivity to applied magnetic fields below 0.5 T [28]. This is in contrast to polycrystalline samples of *o*-$Pr_2Co_3Ge_5$, which were reported to be paramagnetic at an applied field of 1 T [13]. While investigating the flux growth synthesis of *m*-$Pr_2Co_3Ge_5$, we have synthesized single crystals of *o*-$Pr_2Co_3Ge_5$ for the first time and investigated its structure-property relationships to better understand the source of the reported differences in the magnetic properties of these two polymorphs. Here, we report the crystal structure, anisotropic magnetic ordering, thermodynamic properties, and electrical transport behavior of *o*-$Pr_2Co_3Ge_5$. Electron energy loss spectroscopy (EELS) measurements clarify the Pr valence, where it is found to deviate slightly from the trivalent configuration.

2. Methods

Single crystals of *o*-$Pr_2Co_3Ge_5$ were prepared using the flux growth method with Sn as a metallic non-reactive flux. The elements were combined in a ratio of 3 Pr:2 Co:7 Ge:50 Sn. The elements were each transferred to an alumina Canfield crucible [31], then sealed in fused silica tubes under ~1/3 atm of Ar gas. The ampoules were placed in a furnace at 573 K and heated to 1448 K at a rate of 300 K h^{-1}. The samples were dwelled at 1448 K for 6 h, and cooled to 1088 K at a rate of 3 K h^{-1}. The reaction ampoule was removed and immediately centrifuged to remove the excess Sn flux. Residual Sn on the crystal surfaces was removed by etching the crystals in diluted HCl.

Single crystal x-ray diffraction data were obtained at room temperature from a fragment of *o*-$Pr_2Co_3Ge_5$ approximately 0.02 × 0.06 × 0.06 mm^3 in size using a Bruker D8 Quest Kappa single crystal x-ray diffractometer, equipped with an IμS microfocus source (Mo K_α, λ = 0.71073 Å), HELIOS optics monochromator and PHOTON II CPAD detector. The Bruker SAINT program was used to integrate the diffraction data, and the intensities were corrected for absorption via a multi-scan method implemented in SADABS 2016/2 [32]. Preliminary starting models were generated using the intrinsic phasing methods in SHELXT [33] and subsequently anisotropically refined (full-matrix least-square on F^2) using SHELXL [34]. Here, *o*-$Pr_2Co_3Ge_5$ was confirmed to crystallize in the $U_2Co_3Si_5$ structure type (*Ibam*) with lattice parameters a = 9.8199(17) Å, b = 11.9189(9) Å, and c = 5.8592(7) Å. To verify that *Ibam* was the appropriate space group setting, the diffraction data was reprocessed in the monoclinic cell and a refinement was performed in the $Lu_2Co_3Si_5$ structure type (*I*2/c). In *I*2/*c*, the Ge2 atomic site (8 g in space group *Ibam*) will split into the two atomic sites labeled Ge2 and Ge4 (both 4*e* in space group *I*2/*c*). However, when refined in the monoclinic space group, the two Ge sites converge to one unique site which demonstrates that it is more appropriate to adopt the higher symmetry orthorhombic space group. A comparison of the atomic positions for *o*-$Pr_2Co_3Ge_5$ and modeled in *I*2/*c* and *m*-$Pr_2Co_3Ge_5$ from [28] can be found in table S3. Additionally, the angle β was determined to be 90.000 (12)°. For these reasons, the orthorhombic cell was retained. Details of the structure refinement for *o*-$Pr_2Co_3Ge_5$ can be found in tables S1, S2, and S4.

High resolution powder x-ray diffraction data (λ = 0.458 164 Å) were collected in the 2θ range from 0.5° to 50° on a ground single crystal at the 11-BM beamline at the Advanced Photon Source of Argonne National Laboratory. TOPAS was used to perform a Rietveld refinement, identifying *o*-$Pr_2Co_3Ge_5$ as the dominant phase (a = 9.818 94(4) Å, b = 11.917 50(3) Å, and c = 5.858 05(2) Å) with $PrCoGe_3$ as an impurity phase of less than two percent (figure S1). Residual Sn from flux growth and Al_2O_3 from sample preparation were also identified.

A single crystal of *o*-$Pr_2Co_3Ge_5$ was analyzed via energy-dispersive x-ray spectroscopy (EDS) at 20 keV acceleration voltage in a JEOL-IT100 InTouchScope scanning electron microscope equipped with a built in EDS detector in the secondary electron detector mode. The sample was analyzed in three different spots and averaged to a final composition of $Pr_{2.06(9)}Co_{2.92(14)}Ge_{5.03(6)}$.

Magnetic properties measurements were performed on an oriented single crystal using a quantum design vibtrating sample magnetometer magnetic property measurement system. The magnetization measurements were performed at a constant temperature T = 1.8 K under applied magnetic fields (H), from −7 T to 7 T.

For the zero field-cooled and field-cooled magnetic susceptibility measurements, the sample was cooled down to 1.8 K with no applied field before heating to 300 K and cooling back down to 1.8 K with an applied field of $H = 0.2$ T. In both cases, single crystals were mounted such that the magnetic fields were parallel to *a*, *b*, and *c* axes. Heat capacity (C) was measured from 1.8 K to 250 K and electrical resistivity (ρ) from 1.8 K to 300 K using a Quantum Design physical property measurement system. For the electrical resistivity measurements, single crystals were cut into rectangular bars with a general dimension of 0.5 mm by 0.7 mm by 2.0 mm. All surfaces were polished to reduce surface scattering. The measurements were performed in two different orientations, with the electrical current parallel to the *b* and *c* axes.

Electron diffraction patterns were collected in a FEI TitanX operated at 200 kV using a camera-length of 300 mm and a 40 μm select-area aperture. Diffraction patterns were indexed using SingleCrystal [35] based on the distances and angles between Bragg peaks for an orthorhombic *Ibam* unit cell with lattice parameters obtained through single crystal x-ray diffraction. Zone axes were determined based on best fit and minimized sum or the squared errors in distances. The diffraction pattern shown in figure 1(b) confirms that the crystal is orthorhombic and single phase.

EELS was used to determine the electron valency of the Pr atoms. Electron-transparent cross-sections were removed from a bulk $Pr_2Co_3Ge_5$ crystal in a dual-beam Thermo Fischer Scios 2 SEM-FIB. EELS experiments were carried out in the TEAM I aberration-corrected transmission electron microscope equipped with a GIF Continuum operated at an acceleration voltage of 300 kV in the scanning transmission electron microscopy (STEM) configuration. Wien filter monochromation and an energy dispersion of 90 meV channel^{-1} produced an energy resolution of 0.27 eV, increasing the visibility of the fine features in the core-loss spectra. The third condenser lens current was set such that the convergence angle was 20.5 mrad and the probe current was 0.085 nA. Spectral were collected with a K2-IS single electron detector. Dual EELS enabled simultaneous collected of the zero-loss peak (ZLP) in the low energy-loss region and the Pr $M_{4,5}$ core-loss edges. EELS maps were acquired from a 120 nm $\times$ 120 nm region of the sample with a 1 nm step size. All core-loss spectra from the region were summed to increase the signal-to-noise. Using the Gatan DigitalMicrograph package, the core-loss spectra were deconvolved using the ZLP to remove the effects of plural scattering and a power law background subtraction was applied.

3. Results and discussion

3.1. Structure

The structure of *o*-$Pr_2Co_3Ge_5$, shown in figure 1(a), consists of one Pr (8*j*), two Co (8*j*, 4*a*), and three Ge (8*j*, 8*g*, 4*b*) crystallographic sites. The anisotropic features of this structure are highlighted in figure 2. Unlike the other $BaAl_4$ derivatives, $PrCoGe_3$ (*I*4*mm*) and $PrCo_2Ge_2$ (*I*4/*mmm*), the connectivity of the distorted $[Co_2Ge_3]$ tetrahedral slab differs along all crystallographic directions. Along *b*, three configurations of tetrahedron are connected in an A–B–C–B–A pattern, where A is $[CoGe_4]$, B is $[Ge(Ge_2Co_2)]$, and C is $[GeCo_4]$. Along *c*, the configuration of the tetrahedron does not vary, manifesting as continuous rows of Co or Ge atoms. Lastly, *a* is the stacking direction of the $[Co_2Ge_3]$ slabs, which are connected by a Co2-Ge3 dimer (2.3493(8) Å), separating the corrugated layers of Pr atoms across distances between 5.474(7) Å and 5.964(8) Å in length. The crystalline anisotropy of *o*-$Pr_2Co_3Ge_5$ manifest in the magnetic and transport properties.

3.2. Physical properties

Anisotropic temperature dependent magnetic susceptibility $\chi(T)$ data for magnetic fields $H = 0.2$ T applied along the *a*, *b*, and *c* axes are shown in figure 3(a). Curie–Weiss behavior following the expression $\chi(T) = C/T - \theta_{CW}$ is seen for 150 K $< T <$ 300 K and fits to $\chi^{-1}(T)$ are shown in figure 3(b). Results from these fits are summarized in table 1, where the effective magnetic moments along *a*, *b*, and *c* are $\mu_{eff} = 4.01\ \mu_B$ Pr^{-1}, 3.77 μ_B Pr^{-1}, and 4.07 μ_B Pr^{-1}, respectively. These values are larger than the expected value for trivalent Pr ($\mu_{eff} = 3.58\ \mu_B\ (Pr^{3+})^{-1}$), indicating that the Co *d*-electrons contribute to the magnetic moment along all axes. Similar behavior is seen for other $Ln_2Co_3Ge_5$ compounds like $Nd_2Co_3Ge_5$ ($Lu_2Co_3Si_5$-type) and $Sm_2Co_3Ge_5$ ($Lu_2Co_3Si_5$-type) [28], but is absent for others such as *m*-$Pr_2Co_3Ge_5$ ($\mu_{eff} = 3.52\ \mu_B$ Pr^{-1}) [28] and $Tb_2Co_3Ge_5$ ($Lu_2Co_3Si_5$-type) [12]. Anisotropy is also seen in the paramagnetic state, where the Curie–Weiss temperatures $\theta_{CW} = -21.4$ K, -12.5 K, and 9.0 K for H along *a*, *b*, and *c*, respectively. This shows that while there is an antiferromagnetic exchange interaction along the *a* and *b* directions, there are complex ferromagnetic interactions along the *c* direction. At temperatures below the fit range, we observe gradual deviations from the Curie–Weiss behavior that may relate to crystal electric field splitting of the Hund's rule multiplet. Finally, complex magnetic ordering is observed at lower temperatures, where $\chi(T)$ increases abruptly near $T_{sp} = 32$ K by different amounts for H along *a*, *b*, and *c*. This is seen clearly in the temperature derivative of the susceptibility $\partial\chi/\partial T$ as a sharp peak, shown in the

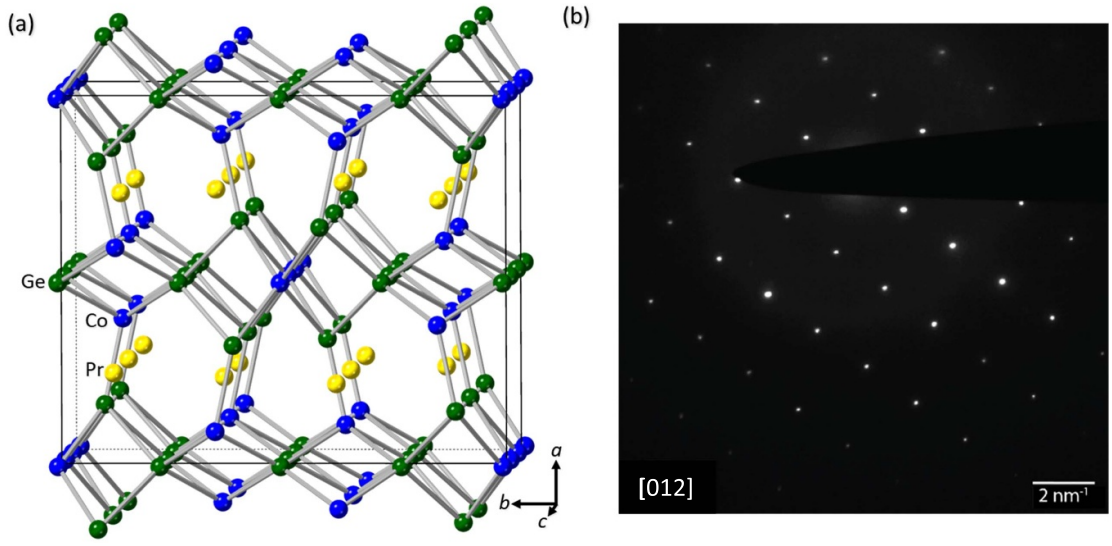

Figure 1. (a) Crystal structure of *o*-$Pr_2Co_3Ge_5$ (*Ibam*), where Pr, Co, and Ge atoms are shown in yellow, blue, and green, respectively. (b) Select-area electron diffraction of a *o*-$Pr_2Co_3Ge_5$ single crystal along [012].

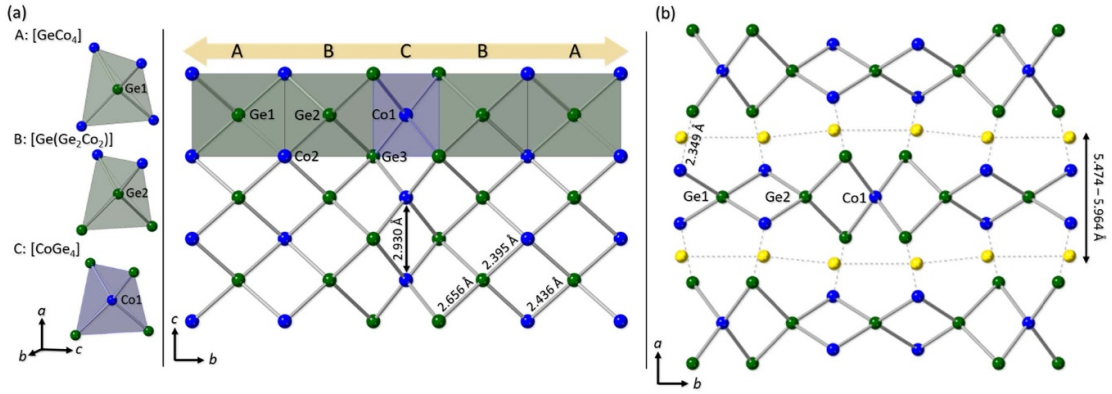

Figure 2. Highlighted crystallographic features of *o*-$Pr_2Co_3Ge_5$, where Pr, Co, and Ge atoms are yellow, blue, and green, respectively. A single tetrahedral slab viewed along *a* is shown in (a) to illustrate the differences in structure along *b* and *c*. The yellow arrow along *c* indicates the A–B–C–B–A arrangement of tetrahedra. The layering of the tetrahedral slabs viewed along *c* in (b) with Pr contacts and Co2-Ge3 dimers shown with dashed grey lines.

inset of figure 3(a). A second anisotropic sub-phase is seen at $T_M = 15$ K, which increases χ for H along c and decreases χ for H along a. It also produces a weak low temperature upturn in χ for H along c at lower temperatures. This reveals that the ground state magnetic configuration is complex, where further measurements will be needed to identify the detailed order parameter. A second possibility is that that the low temperature features stem from magnetic impurities; however, no evidence of this was observed in single crystal x-ray diffraction. Our results are contrasted with an earlier study of polycrystalline *o*-$Pr_2Co_3Ge_5$, which exhibits paramagnetic behavior where fits to the data yield $\mu_{eff} = 3.76\ \mu_B\ Pr^{-1}$, $\theta_{CW} = 5.48$ K, and little evidence for magnetic ordering [13].

Further insights about the magnetically ordered state are obtained from anisotropic field dependent magnetization measurements $M(H)$ for $H < 7$ T shown in figure 3(c). For fields along the c axis, $M(H)$ increases abruptly to $M = 0.9\ \mu_B$ F.U.$^{-1}$ near zero field with a small hysteresis loop, and then gradually saturates towards a value near 4 μ_B F.U.$^{-1}$ This shows that there is a spontaneous magnetization within the ordered state that is consistent with there being a partial spin-polarization along the c direction. We also compare the extrapolated saturation moment with the Hund's rule value $M_{sat} = 3.2\ \mu_B\ (Pr^{3+})^{-1}$. This shows that the extrapolated saturation moment per Pr ($M_{sat} = 1.83\ \mu_B\ Pr^{-1}$) is reduced from the Hund's rule value, consistent with there being crystal electric field splitting that reduces the ground state moment. In contrast, the increase in $M(H)$ is more gradual along a and b and we note (a) that these curves are not perfectly linear and (b) are suppressed from the values for H along c. This leads us to anticipate that the application of larger magnetic fields in these directions would drive metamagnetic phase transitions. Similar magnetization was

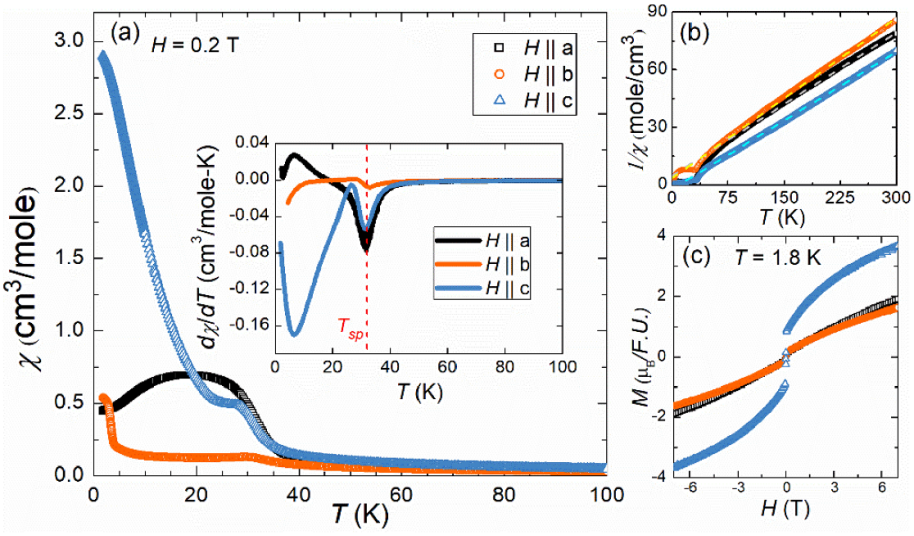

Figure 3. (a) Anisotropic temperature-dependent magnetic susceptibility $\chi(T)$ of o-$Pr_2Co_3Ge_5$ measured under an applied magnetic field of $H = 0.2$ T. The inset in (a) is the derivative of the magnetic susceptibility with respects to temperature, where the dashed red line indicates the first magnetic transition temperature T_{sp}. (b) Inverse of the magnetic susceptibility vs temperature, where the dashed lines represent the Curie–Weiss fit. (c) Anisotropic magnetization M vs applied magnetic field H measured at $T = 1.8$ K.

Table 1. Summarized magnetic data for o-$Pr_2Co_3Ge_5$.

	μ_{eff} (μ_B Pr^{-1})	θ_{CW} (K)	T_{sp} (K)	T_M (K)
H // a	4.01	−21.36	∼32	—
H // b	3.77	−12.50	∼32	<5
H // c	4.07	9.04	∼32	<15

reported in $Pr_2Ni_3Si_5$ ($U_2Co_3Si_5$-type) [10, 36] and $Pr_2Ni_3Ge_5$ ($U_2Co_3Si_5$-type) [20]. Neutron diffraction is needed to understand the nature of the anisotropic magnetic behavior of o-$Pr_2Co_3Ge_5$.

Zero-field electrical resistivity $\rho(T)$ curves measured for electrical currents applied parallel to b and c are shown in figure 4. Metallic behavior is observed, where both curves decrease gradually from room temperature with a slight negative curvature. Similar behavior was previously seen for the polycrystalline specimens and is not unusual for lanthanide-based intermetallics that contain d-electron elements. For example, the filled skutterudites $LaRu_4As_{12}$ and $PrRu_4As_{12}$ show related behavior where the temperatures dependence of the electrical resistivity is determined by a combination of the Bloch–Gruneisen formula and scattering of s-electrons into incompletely filled d-bands [37]. We also note that the resistivity parallel to b, along which the tetrahedral configurations vary, is approximately three times that of the resistivity along c. This illustrates the differences in connectivity of the $[Co_3Ge_5]$ slab and likely relates to the Fermi surface anisotropy. Finally, for current applied along b, a kink is seen near T_{sp} which is followed by a gradual decrease with decreasing T. The transition is less clear for current along c, which reveals that the extent to which the electronic scattering is reduced by the magnetic ordering is anisotropic. We also find that there is no obvious feature near T_M.

The temperature dependent heat capacity $C(T)$ are summarized in figure 5. The data resemble what is seen for polycrystalline specimens [13] and are well described by a Debye–Einstein model [38] for 50 K < T < 300 K,

$$C(T) = C_D\,(T/\theta_D)^3 \int_0^{\theta_D/T} \frac{x^4 e^x}{(e^x-1)^2}dx + C_E(\theta_E/T)^2 \frac{\left(e^{\theta_E/T}\right)}{\left(e^{\theta_E/T}-1\right)^2}, \quad (1)$$

where $x = \frac{\hbar\omega}{\kappa_B T}$, ω is the Debye frequency, θ_D and θ_E are the Debye and Einstein temperatures, respectively, and C_D and C_E are constants containing n umbers of oscillators and degrees of freedom, respectively [39]. The resulting Debye temperature $\theta_D = 222$ K is comparable to that of the non-magnetic analog $La_2Co_3Ge_5$ $\theta_D = 282$ K [40], which suggests that our model is a good representation of the non-magnetic contribution to the specific heat. We also note that a simple Debye function (blue dotted curve) does not describe the data as well, which implies that it is appropriate to include an Einstein term. Although it remains to be

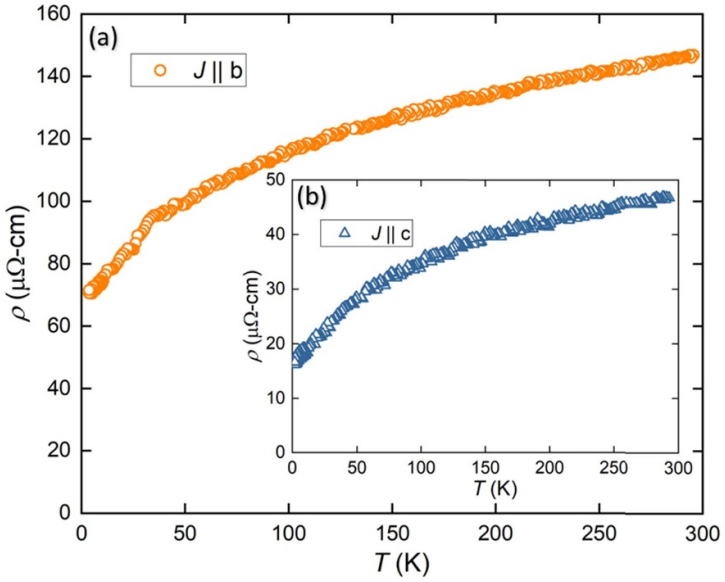

Figure 4. Temperature-dependent electrical resistivity of $Pr_2Co_3Ge_5$ measured in two different orientations, with electrical current (a) parallel to *b*-axis and (b) parallel to *c*-axis.

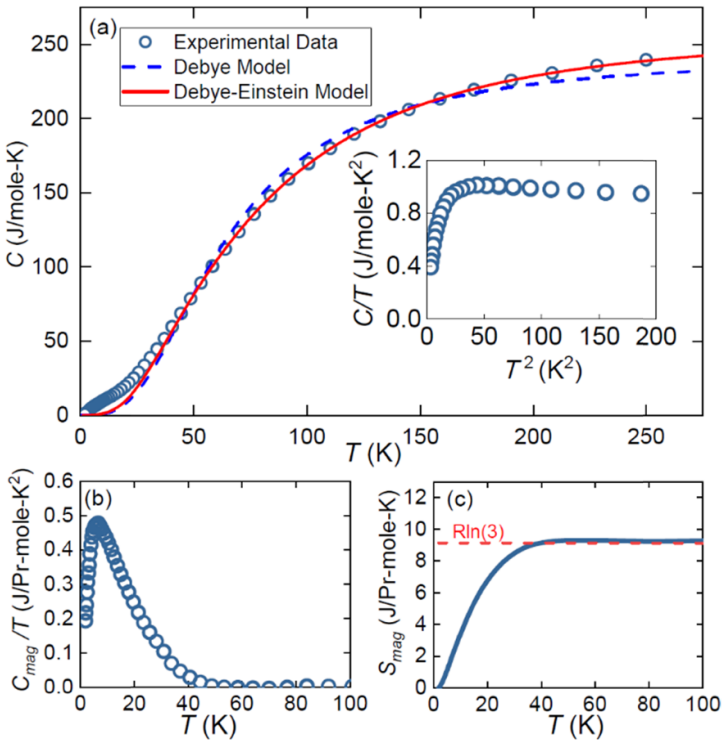

Figure 5. Temperature-dependent (a) specific heat $C(T)$. The dashed and solid lines represent the high temperature fittings using the Debye and Debye–Einstein models as described in the text. The inset represents the low-temperature behavior plotted as C/T vs T^2, (b) magnetic contribution to the heat capacity over temperature per mole of Pr, and (c) magnetic entropy per mole of Pr (S_{mag}) of $Pr_2Co_3Ge_5$.

established, we speculate that this may originate from the large mass of Pr ions which are contained within distorted Co-Ge cages. At temperatures below 50 K there is a pronounced deviation from the lattice behavior, which could originate from splitting of the Hund's rule multiplet by the crystal electric field (i.e. a Schottky anomaly) [1, 13, 16, 21, 39, 40] or represent spin fluctuations and magnetic ordering of the Pr *f*-electron magnetic moments. To isolate this term, we subtract the Debye–Einstein fit from the data, which yields the curve C_{mag}/T shown in figure 5(b). Fits to the data using a two level Schottky model were attempted but were unsuccessful. We also note that the weight of C_{mag}/T spans the ordering temperatures T_{sp} and T_M, which

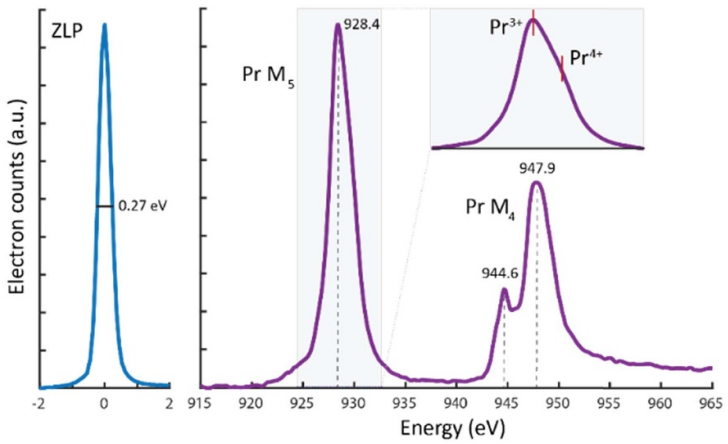

Figure 6. Monochromated STEM-EELS of Pr $M_{4,5}$ edges collected from a 150 N m^2 region of *o*-$Pr_2Co_3Ge_5$. From the zero-loss peak, the energy-resolution is 0.27 eV. The Pr M_4 edge has peaks at 944.6 eV and 947.9 eV, corresponding to Pr^{3+} and Pr^{4+} oxidation states, respectively. Similarly, the Pr M_5 edge has a main peak at 928.4 eV and a shoulder feature at 929.5 eV, corresponding to Pr^{3+} and Pr^{4+}, respectively. From the spectra, the bulk average Pr valency is dominated by the Pr^{3+} cation.

suggests that this part of the heat capacity is associated with the magnetic ordering. However, we cannot rule out the possibility that a Schottky anomaly also contributes over this temperature range. Finally, the magnetic entropy S_{mag} shown in figure 5(c) is obtained using the expression $S_{mag} = \int_0^T \frac{C_{mag}}{T} dT$ [41]. We find that S_{mag} saturates towards a value near $R\ln 3$ near 40 K, which is smaller than the theoretical value for the complete Hund's rule multiplet of trivalent Pr ($J = 4$) [42], $-\Delta S_{max} = Rln(2J+1) = Rln(9)$, where R is the gas constant. This shows that crystal electric field splitting impacts the magnetic ground state at temperatures above 40 K, but still does not rule out the possibility that additional splitting occurs with the same energy scale as the magnetic ordering. A magnified plot of the region from 2 K to 50 K for both the magnetic contribution to the specific heat and magnetic entropy are provided in figure S2.

3.3. Electron energy loss spectroscopy

The ZLP and Pr $M_{4,5}$ edges collected using monochromated STEM EELS are shown in figure 6. The width of the ZLP at half of its maximum height is 0.27 eV, giving the energy resolution of the spectra. The $M_{4,5}$ edges result from the excitation of 3*d* core electrons to the unoccupied 4*f*-states ($3d^{10}4f^n \rightarrow 3d^9 4f^{n+1}$), in the lanthanides [43]. The sharp M_5 peak at 928.4 and M_4 peak at 947.9 eV correspond to dipole-permitted transitions from the Pr $3d^{5/2}$ and $3d^{3/2}$ core levels into the $4f^{7/2}$ and $4f^{5/2}$ states, respectively [44]. Both M_4 and M_5 edges split into two peaks, with the lower energy-loss peak corresponding to the Pr^{3+} cation and the higher energy-loss peak corresponding to the Pr^{4+} cation. The splitting of $M_{4,5}$ edge into two separate peaks corresponding to Pr^{3+} and Pr^{4+} results from the high probabilities of two electron transition pathways to available final states and coupling between final and initial states [45]. The split is more apparent for the M_4 edges, but the inset in figure 6 shows a shoulder feature on the higher-energy side of the M_5 edge. Based on comparison with x-ray absorption spectra [46, 47] and consideration of the $M_{4,5}$ edge features, the spectrum indicates that the mean Pr valence is overwhelmingly Pr^{3+} although a small proportion of Pr^{4+} is likely present in the sample. Compared to Pr^{4+}, Pr^{3+} contains more outer-shell electrons, resulting in greater relative core-hole screening and looser core electron bonding, which is responsible for the lower energy-loss of Pr^{3+} compared to Pr^{4+} in the EEL spectra [46]. The dominant Pr^{3+} state agrees with the results obtained through magnetic susceptibility measurements. The relatively small contribution of the Pr^{4+} state, correspond well with the report of a mixed valence state in $Ce_2Co_3Ge_5$ [13], as one would expect less 4*f* hybridization with the conduction band in Pr analogues compared to Ce. Additionally, in $U_2Rh_3Si_5$ ($Lu_2Co_3Si_5$-type) and $U_2Ir_3Si_5$ ($U_2Co_3Si_5$-type) [15], x-ray absorption spectroscopy has shown an intermediate U valence state close U^{4+}. The nature of the Pr 4*f* state could have strong implications for the highly correlated nature of *o*-$Pr_2Co_3Ge_5$ and related phases should be investigated further.

4. Conclusion

Single crystals of *o*-$Pr_2Co_3Ge_5$ ($U_2Co_3Si_5$-type) were grown using Sn flux and its physical properties were investigated anisotropically for the first time. Magnetic susceptibility measurements at 0.2 T revealed anisotropic Curie–Weiss paramagnetism consistent with trivalent Pr ions. Magnetic ordering occurs at

approximately $T_{sp} = 32$ K and a second spin reorientation occurs along the *b* and *c* directions near $T_M = 15$ K. In the paramagnetic state, dominant antiferromagnetic interactions were observed along the *a* and *b* directions, whereas *c* was found to have complex ferromagnetic interactions. A broad magnetic contribution to the specific heat was observed near T_{sp} due to either a Schottky anomaly or spin fluctuations. EELS has indicated the presence of a dominant Pr^{3+} valence state with a minor Pr^{4+} contribution. This indicates that there is an instability of the *f*-electron valence that might be favorable for strong electronic correlations. Future investigations of the electronic and magnetic structure are needed to clarify the highly correlated nature of *o*-$Pr_2Co_3Ge_5$. Additionally, further studies are underway to elucidate the structural and property relationships between *o*-$Pr_2Co_3Ge_5$ and *m*-$Pr_2Co_3Ge_5$.

Data availability statement

The data that support the findings of this study are openly available at the following URL/DOI: https://www.ccdc.cam.ac.uk/structures/ for the single crystal structure of *o*-$Pr_2Co_3Ge_5$ under deposition number CSD 2174502.

Acknowledgments

J Y C gratefully acknowledges the support of the Welch Foundation (AT-2056-20210327) and the U.S. Department of Energy (DE-SC0022068). This material is based upon work supported by the U.S. Department of Energy, Office of Science, Office of Workforce Development for Teachers and Scientists, Office of Science Graduate Student Research (SCGSR) program. The SCGSR program is administered by the Oak Ridge Institute for Science and Education for the DOE under Contract No. DE-SC0014664. R B was supported by the National Science Foundation through NSF DMR-1904361. The National High Magnetic Field Laboratory is supported by the National Science Foundation through NSF DMR-1644779 and the State of Florida. This research used resources of the Advanced Photon Source; a U.S. Department of Energy (DOE) Office of Science user facility operated for the DOE Office of Science by Argonne National Laboratory under Contract No. DE-AC02-06CH11357. We are grateful to Saul Lapidus for his helpful suggestions and conversation. Transmission electron microscopy was performed at the Molecular Foundry at Lawrence Berkeley National Laboratory. Work at the Molecular Foundry was supported by the Office of Science, Office of Basic Energy Sciences, of the U.S. Department of Energy under Contract No. DE-AC02-05CH11231.

ORCID iDs

Trent M Kyrk https://orcid.org/0000-0003-0810-5782
Kaya Wei https://orcid.org/0000-0003-0912-9380
Ryan E Baumbach https://orcid.org/0000-0002-6314-3629
Julia Y Chan https://orcid.org/0000-0003-4434-2160

References

[1] Bugaris D E *et al* 2017 *J. Am. Chem. Soc.* **139** 4130
[2] Kuo C N, Hsu C J, Tseng C W, Chen W T, Lin S Y, Liu W Z, Kuo Y K and Lue C S 2020 *Phys. Rev.* B **101** 155140
[3] Singh Y, Pal D and Ramakrishnan S 2004 *Phys. Rev.* B **70** 064403
[4] Singh Y and Ramakrishnan S 2004 *Phys. Rev.* B **69** 174423
[5] Sung N H, Roh C J, Kim K S and Cho B K 2012 *Phys. Rev.* B **86** 224507
[6] Piraux L, Grivei E, Chevalier B, Dordor P, Marquestaut E and Etourneau J 1993 *J. Magn. Magn. Mater.* **128** 313
[7] Hossain Z, Ohmoto H, Umeo K, Iga F, Suzuki T, Takabatake T, Takamoto N and Kindo K 1999 *Phys. Rev.* B **60** 10383
[8] Singh Y and Ramakrishnan S 2003 *Phys. Rev.* B **68** 054419
[9] Chevalier B, Roisnel T and Etourneau J 1994 *J. Magn. Magn. Mater.* **134** 88
[10] Mazumdar C, Nagarajan R, Gupta L C, Vijayaraghavan R, Godart C and Padalia B D 1994 *IEEE Trans. Magn.* **30** 4960
[11] Bugaris D E, Malliakas C D, Bud'ko S L, Calta N P, Chung D Y and Kanatzidis M G 2017 *Inorg. Chem.* **56** 14584
[12] Remya U D, Arun K, Swathi S, Dzubinska A, Reiffers M and Nagalakshmi R 2021 *J. Alloys Compd.* **889** 161536
[13] Layek S, Anand V K and Hossain Z 2009 *J. Magn. Magn. Mater.* **321** 3447
[14] Sarkar S, Subbarao U, Joseph B and Peter S C 2015 *J. Solid State Chem.* **225** 181
[15] Honda F *et al* 2020 Magnetic and electronic properties of the ternary compound $U_2T_3Si_5$ (T = Rh, Ir) *Proc. J-Physics 2019: Int. Conf. Multipole Physics and Related Phenomena* (https://doi.org/10.7566/JPSCP.29.013002)
[16] Sanki S *et al* 2022 *Phys. Rev.* B **105** 165134
[17] Nakashima M, Kohara H, Thamizhavel A, Matsuda T D, Haga Y, Hedo M, Uwatoko Y, Settai R and Ōnuki Y 2005 *J. Phys.: Condens. Matter* **17** 4539
[18] Gouchi J, Nakamura Y, Nakashima M, Amako Y, Kumar R and Uwatoko Y 2018 *AIP Adv.* **8** 101323
[19] Venturini G, Méot-Meyer M, Marêché J F, Malaman B and Roques B 1986 *Mater. Res. Bull.* **21** 33
[20] Anand V K, Nandy A K, Dhar S K, Geibel C and Hossain Z 2007 *J. Magn. Magn. Mater.* **313** 164
[21] Anand V K, Hossain Z and Geibel C 2008 *Phys. Rev.* B **77** 184407

[22] Sheng Q, Zhang J, Huang K, Ding Z, Peng X, Tan C and Shu L 2017 *Chin. Phys.* B **26** 057401
[23] Kaushik V, Venkateshwarlu D, Mishra A K, Krishnan M, Venkatesh R, Patidar M M and Ganesan V 2019 *Physica* B **570** 296
[24] Kaushik V and Ganesan V 2021 *J. Alloys Compd.* **888** 161592
[25] Bodak O I, Kotur B Y, Yarovets V I and Gladyshevskii E I 1977 *Kristallografiya* **22** 385
[26] Aksel'rud L G, Yarmolyuk Y P and Gladyshevskij E I 1977 *Kristallografiya* **22** 861
[27] Chabot B and Parthé E 1985 *J. Less-Common Met.* **106** 53
[28] Kyrk T M, Scheifers J P, Thanabalasingam K, McCandless G T, Young D P and Chan J Y 2021 *Inorg. Chem.* **60** 15343
[29] Morozkin A V 2012 *Intermetallics* **25** 136
[30] Fedyna M, Pecharskii V and Bodak O 1987 *Inorg. Mater.* **23** 570
[31] Canfield P, Kong T, Kaluarachchi U and Jo N H 2016 *Phil. Mag.* **96** 84
[32] Krause L, Herbst-Irmer R, Sheldrick G M and Stalke D 2015 *J. Appl. Crystallogr.* **48** 3
[33] Sheldrick G M 2015 *Acta Crystallogr.* A **71** 3
[34] Sheldrick G M 2015 *Acta Crystallogr.* C **71** 3
[35] Palmer D C 2015 Visualization and analysis of crystal structures using CrystalMaker Software *Z. Kristallogr. - New Cryst. Struct.* **230** 559–72
[36] Mazumdar C, Nigam A K, Nagarajan R, Gupta L C, Godart C, Padalia B D, Chandra G and Vijayaraghavan R 1996 *Phys. Rev.* B **54** 6069
[37] Sayles T A, Baumbach R E, Yuhasz W M, Maple M B, Bochenek Ł, Wawryk R, Cichorek T, Pietraszko A, Henkie Z and Ho P-C 2010 *Phys. Rev.* B **82** 104513
[38] Kittel C 1967 *Introduction to Solid State Physics* 3rd edn (New York: Wiley) p 648
[39] Ramakrishnan S, Patil N G, Chinchure A D and Marathe V R 2001 *Phys. Rev.* B **64** 064514
[40] Anand V K, Anupam G, Hossain Z, Ramakrishnan S, Thamizhavel A and Adroja D T 2012 *J. Magn. Magn. Mater.* **324** 2483
[41] Ashcroft N W and Mermin N D 1976 *Solid State Physics* (Philadelphia, PA: Saunders College Publishing) p 797
[42] Blundell S 2001 *Magnetism in Condensed Matter* (Oxford: Oxford University Press) p 238
[43] Manoubi T, Colliex C and Rez P 1990 *J. Electron Spectrosc. Relat. Phenom.* **50** 1
[44] Crecelius G, Wertheim G K and Buchanan D N E 1978 *Phys. Rev.* B **18** 6519
[45] Merzbacher E 1998 *Quantum Mechanics* 3rd edn (New York: Wiley)
[46] Zhuravleva M, Friedrich S and Melcher C L 2012 *Appl. Phys. Lett.* **101** 101902
[47] Lu Q, Vardar G, Jansen M, Bishop S R, Waluyo I, Tuller H L and Yildiz B 2018 *Chem. Mater.* **30** 2600